Ma *et al. Journal of Nanobiotechnology* (2025) 23:248
https://doi.org/10.1186/s12951-025-03336-8

Journal of Nanobiotechnology

RESEARCH **Open Access**

Dual-modality immune nano-activator harnessing Mn^{2+} and quercetin to potentiate the cGAS-STING pathway for advanced cancer metalloimmunotherapy

Shanshan Ma[1†], Xuequan Zhang[2†], Xiaoqi Zhu[1†], Kangning Yan[1,4], Qin Wang[1,4], Lei Lei[2], Jiasheng Li[5], Jing Guo[1], Weizhong Tang[5], Junjie Liu[1], Jun Cao[2*], Duo Wang[3*] and Tao Luo[5*]

Abstract

Manganese ions (Mn^{2+}) have emerged as promising activators of the cyclic GMP-AMP synthase-stimulator of interferon genes (cGAS-STING) pathway. However, their clinical application was hindered by low bioavailability and limited immune activation pathways, which impaired their ability to trigger robust immune responses and achieve significant antitumor effects. To address these challenges, we developed a dual-modality immune nano-activator by coordinating manganese ions with quercetin. This strategy was designed to enhance the cGAS-STING pathway activation and elicit the immunogenic cell death, thereby strengthening the antitumor immune response. The engineered nano-activator demonstrated superior tumor-targeting ability and efficient cellular internalization. Upon exposure to near-infrared irradiation, the system harnessed photothermal effects to induce apoptosis in tumor cells while simultaneously accelerating the release of manganese ions and quercetin. The released manganese ions facilitated the generation of reactive oxygen species, which in conjunction with quercetin-induced apoptosis, amplified photothermal-induced DNA damage. This DNA damage further promoted the release of cytosolic DNA, which in turn activated the cGAS-STING pathway, thereby intensifying immune activation. Notably, the nano-activator also triggered immunogenic cell death, which synergized with the cGAS-STING activation to promote dendritic cell maturation and activate antigen-specific T-cell, significantly enhancing the immune response against the tumor. Both in vitro and in vivo studies confirmed that this nano-activator effectively inhibited tumor growth, with particularly pronounced effects when combined with anti-CTLA-4 antibodies.

Keywords cGAS-STING, Quercetin, Manganese ions, Photothermal therapy, Metalloimmunotherapy

---

†Shanshan Ma, Xuequan Zhang and Xiaoqi Zhu have contributed equally to this work.

*Correspondence:
Jun Cao
caojun@scu.edu.cn
Duo Wang
wangduo2022@126.com
Tao Luo
luotao@gxmu.edu.cn
Full list of author information is available at the end of the article

Graphical abstract

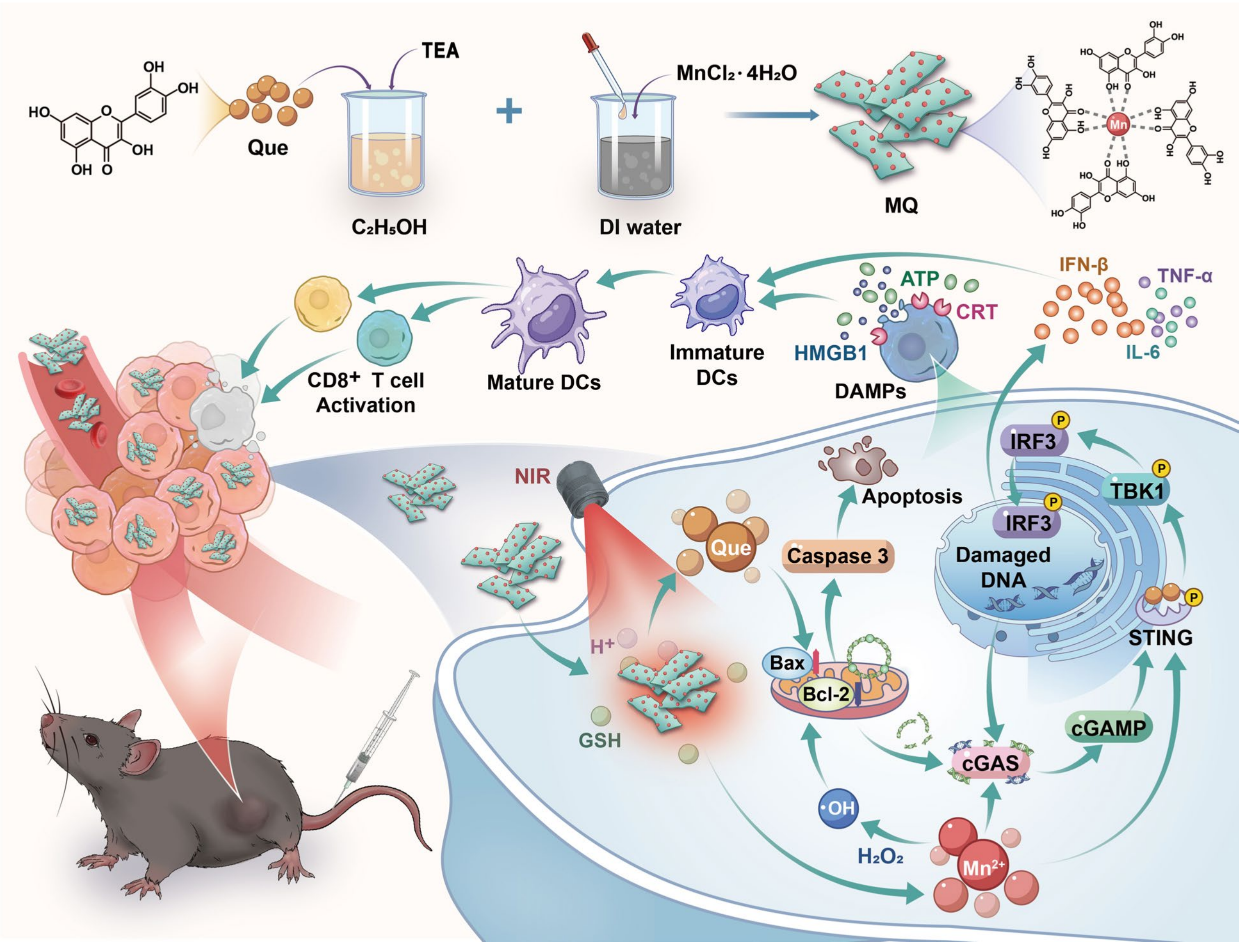

Introduction

The emergence of immune checkpoint inhibitors and chimeric antigen receptor T-cell (CAR-T) therapies has significantly revolutionized cancer treatment [1, 2]. Cancer immunotherapy not only activated an immune response against tumor but also had the potential to inhibit tumor growth, recurrence and metastasis [3–6]. Despite these revolutionary advances, significant challenges persisted in clinical practice, particularly within the tumor immunosuppressive microenvironment (TME), where the efficacy of immunotherapy was often severely compromised. The TME utilized multiple mechanisms, such as promoting T-cell exhaustion, secreting immunosuppressive cytokines, and inducing the polarization of tumor-associated macrophages (TAMs) into an M2 phenotype, all of which collectively suppressed the antitumor immune response and significantly hindered the effectiveness of immunotherapy [7]. Currently, activating key innate immune pathways—particularly the cyclic GMP-AMP synthase-stimulator of interferon genes (cGAS-STING) pathway—has emerged as a promising strategy to enhance antitumor immune responses [8–17]. The cGAS-STING pathway was activated by the recognition of cytosolic DNA, which triggered the production of type I interferons (IFN-I) and initiated innate immune responses. This activation not only triggered the innate immune system but also facilitated the subsequent activation of adaptive immune responses, thereby enhancing antitumor immunity [18–22]. Given its ability to regulate both innate and adaptive immunity, the cGAS-STING pathway has become an attractive target in cancer immunotherapy. However, current cGAS-STING agonists, including natural cyclic dinucleotides (CDNs) [23, 24] and synthetic small-molecule agonists [25], had limitations related to delivery efficiency, stability, and safety, which impeded their clinical application [26, 27]. Furthermore, effective activation of the cGAS-STING pathway is highly dependent on cytosolic DNA signaling, adding further complexity to its regulation.

In recent years, manganese ions (Mn^{2+}) have garnered attention as a novel cGAS-STING pathway agonist due to their unique biological effects [28]. Studies have demonstrated that Mn^{2+} can significantly enhance the sensitivity of cGAS to cytosolic DNA, thereby amplifying the STING signaling pathway and promoting the secretion of key immune factors such as interferon-β (IFN-β), which in turn triggered robust antitumor immune responses [29, 30]. Moreover, Mn^{2+} can induce Fenton-like reactions within cells, generating reactive oxygen species (ROS) [31, 32]. These ROS not only facilitated chemodynamic therapy (CDT) [33–35] but also induced immunogenic cell death (ICD) [36, 37], leading to a dual enhancement of immune activation and therapeutic efficacy. However, the rapid clearance of Mn^{2+} in vivo, along with its nonspecific distribution and the neutralization of ROS by the high concentration of glutathione (GSH) within tumor cells, limited the effectiveness of immune activation. These challenges have driven the development of Mn^{2+} delivery strategies, particularly through nanostructured platforms designed to enable targeted delivery and sustained release of Mn^{2+} within the TME, thereby enhancing its antitumor immunoactivity.

Metal coordination polymers, a class of multifunctional nanomaterial, have shown considerable potential in cancer therapy [38, 39]. These materials usually possessed unique porous structures, high drug-loading capacities, tunable surface chemistries, and favorable biocompatibility, making them ideal candidates for the delivery of Mn^{2+} and other anticancer agents [40–42]. Specifically, Mn^{2+}-based coordination polymers not only retained the immune-stimulatory properties of Mn^{2+} but also exhibited photothermal effects under near-infrared (NIR) irradiation, further promoting tumor cell apoptosis and enhancing immune activation. Quercetin (Que), a natural flavonoid, has garnered significant attention for its anticancer properties and its ability to regulate multiple signaling pathways [43–45]. However, its poor water solubility and low bioavailability limited its clinical applications [46]. By coordinating Que with Mn^{2+} to form a coordination polymer that integrated photothermal effects with immune activation capabilities, these challenges can be addressed. This innovative strategy not only preserved the individual advantages of each component but also enhanced their synergistic immune-stimulating potential, offering promising new avenues for cancer immunotherapy.

Building on these insights, we have proposed to design a dual-modality immune nano-activator (MQ) the coordination of Mn^{2+} and Que, aimed at enhancing the activation of cGAS-STING pathway to potentiate antitumor immune responses. This nano-activator exhibited excellent tumor-targeting capabilities and improved cellular uptake efficiency. Upon near-infrared (NIR) irradiation, the system induced tumor cell apoptosis via photothermal effects while simultaneously facilitating the release of manganese ions and Que. This combination substantially enhanced DNA damage and promoted the release of cytosolic DNA, thereby amplifying the activation of cGAS-STING pathway. Furthermore, the engineered MQ nano-activator triggered ICD, which, in combination with cGAS-STING pathway activation, promoted dendritic cell (DC) maturation and antigen-specific T-cell activation, ultimately leading to a significant improvement in immunotherapeutic efficacy (Scheme 1). Both in vitro and in vivo studies have demonstrated that the engineered MQ effectively inhibited tumor growth, particularly when combined with immune checkpoint inhibitors such as anti-CTLA-4 antibodies.

Materials and methods

Materials

Manganese chloride tetrahydrate ($MnCl_2·4H_2O$) was purchased from Titan Scientific Co.Ltd (Shanghai, China). Quercetin (Que) was purchased from Huaxia Chemical Reagent Co., Ltd (Chengdu, China). Triethylamine was purchased from Aladdin Reagent Co., Ltd. (Shanghai, China). 3,3′,5,5′-tetramethyl-benzidine (TMB) was obtained via Solarbio Science & Technology Co., Ltd (Beijing, China). Anhydrous ethanol was procured from Chengdu Kelong Chemical Co., Ltd. ATP Assay Kit and Cy3-labeled secondary antibodies were bought from Beyotime Biotechnology Inc. Transwell® with 8.0 μm Pore Polycarbonate Membrane Insert and Corning® Matrigel® Basement Membrane Matrix were provided by Corning Incorporated Company provided. Fluorescent secondary antibody conjugated with DyLight™ 680 was procured from Cell Signaling Technology. RIPA lysis buffer, phosphatase inhibitor cocktail, Western blot (WB) transfer buffer, and QuickBlock™ blocking buffer were obtained from Beyotime Biotechnology Inc. Tricolor Prestained Protein Ladder, PAGE gel rapid preparation kit (10%) and PAGE gel rapid preparation kit (12.5%) were supplied by Epizyme Biomedical Technology Co., Ltd. Hoechst 33342 and 2-(4-amidinophenyl)−6-indolecarbamidine dihydrochloride (DAPI) were purchased from Solarbio Science and Technology Co., Ltd., while Bromethol was acquired from EasyCheck Nanjing AIBI Biotechnology Co., Ltd. Triton X-100 and 4% paraformaldehyde were sourced from Biosharp Biotechnology Co., Ltd. The Annexin

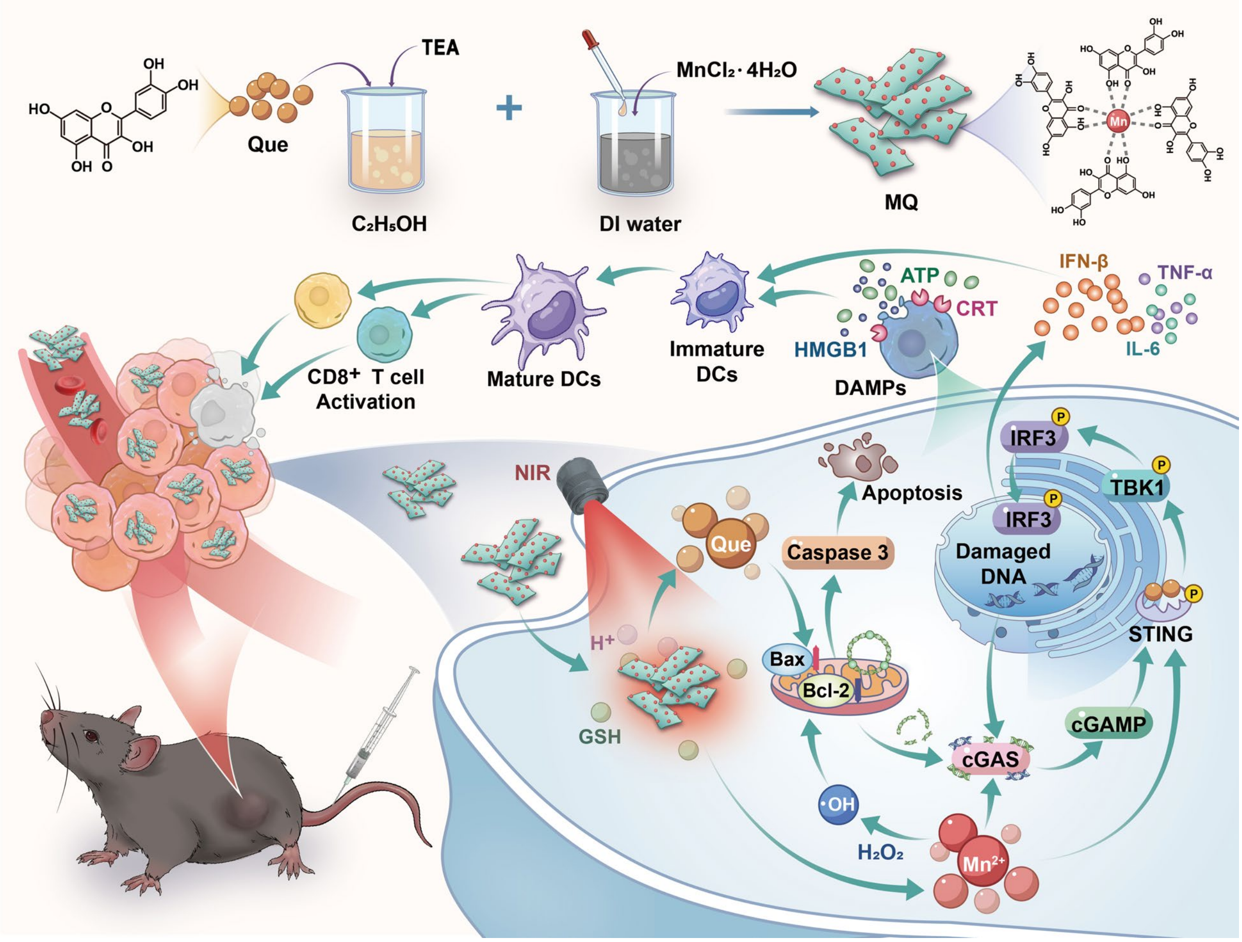

Scheme 1 Schematic illustration of the synthesis and antitumor mechanisms of the MQ nano-activator. The process began with the synthesis of metal coordination polymer (MQ). Followed by MQ induced cGAS-STING pathway activation and trigger immunogenicity cell death (ICD), which together enhance the overall diagram of antitumor immune responses

V-FITC apoptosis detection kit and mitochondrial membrane potential assay kit with JC-1 were procured from BestBio Biotechnology Co., Ltd. Calcein AM/PI assay kit and DCFH-DA probes were obtained from Beyotime Biotechnology Inc (Shanghai, China). Mouse IL-6 ELISA Kit, mouse TNF-α ELISA Kit, mouse IFN-β ELISA kit, and mouse IFN-γ amag ELISA kit were purchased from NeoBioscience Biotechnology Co., Ltd. PerCP/Cyanine5.5 anti-mouse CD3 Antibody, APC anti-mouse/human CD11c Antibody and APC anti-mouse CD8 Antibody were all purchased from BioLegend. HMGB1 Rabbit mAb, CRT Rabbit mAb, Bcl-2 Rabbit mAb, Bax Rabbit mAb, TBK1/NAK Rabbit mAb, IRF3 Rabbit mAb and β-actin Rabbit mAb and Phospho-IRF3 Antibody were supplied by ABclonal Technology Co., Ltd. Phospho-TMEM173/STING Antibody and Phospho-TBK1 Antibody were procured from Affinity Biosciences. Histone γ-H2AX Polyclonal antibody, TMEM173/STING Polyclonal antibody, CD86 Monoclonal Antibody, CD80 Monoclonal Antibody and cGAS Polyclonal antibody were sourced from Proteintech Group, Inc. Mouse cGAMP ELISA kit was purchased from Jiangsu Meimian Industrial Co., Ltd.

Liver cancer cells line Hepa1-6, Hepa1-6 (Luc1) and Mouse bone marrow-derived dendritic cells DC2.4 were purchased from Zhejiang Meisen Technology Co. Ltd. THLE-2 cells were derived from the American Type Culture Collection. Hepa1-6 (Luc1) cells and Hepa1-6 cells were cultured in Dulbecco's modified Eagle's medium (DMEM) supplemented with 10% FBS and 1% penicillin-streptomycin, under humid conditions of 37 °C and 5% CO_2. C57BL/6 mice (4-week-old) were sourced from the Experimental Animal Center of Guangxi Medical University. The animal experiments were maintained and approved by Guangxi Medical University Cancer Hospital's Ethical Committee.

Synthesis of dual-modality immune nano-activator

To synthesize the immune nano-activator (MQ), a 79 mg/mL aqueous solution of $MnCl_2 \cdot 4H_2O$ (62.5 µL) was diluted with deionized water to a final volume of 5 mL, serving as the manganese precursor. Subsequently, Que (1 mg) was dissolved in anhydrous ethanol (1 mL) and mixed with triethylamine (TEA) (50 µL). The resulting Que solution was slowly added dropwise into the manganese precursor and stirred overnight. After that, the suspension was purified by dialysis (Mw: 1000 Da) to remove unreacted precursors and byproducts, resulting in the purified nano-activators (MQ).

Characterization of dual-modality immune nano-activator

The particle size and zeta potential of MQ were measured by dynamic light scattering (DLS, 90Plus PALS, Brookhaven, UK). The morphology of MQ was observed by transmission electron microscopy (TEM, Talos F200S, USA). UV–Vis spectra were recorded using a Microplate Reader (Victor NivoTM, PerkinElmer, USA). FT-IR spectra were obtained with FT-IR spectroscopy (Spectrum Two, PerkinElmer, USA). The valence state of Mn was assessed using an X-ray photoelectron spectrometer (XPS, AXIS ULTRA DLD, Kratos, Britain). The Mn content in MQ was measured with an inductively coupled plasma optical emission spectrometer (ICP-OES, Agilent 7800, USA). In addition, to evaluate the stability of MQ, different media were used to simulate the environment, including H_2O and 10% fetal bovine serum (FBS) in PBS (10 mM, pH = 7.4). MQ was dispersed in these media, and changes in size over time was monitored by DLS.

Release behaviors of MQ

To investigate the release behavior of manganese ions in MQ, the HEPES (pH 7.4), HEPES with 10 mM H_2O_2 (pH = 5.0) were used to simulate tumor environments in vivo. 1 mL MQ was added into a dialysis bag (Mw: 3500 Da), which was then placed in 10 mL of the release medium with and without NIR irradiation. The bag was dialyzed at 37 °C with shaking at 100 rpm. At predetermined time, 10 mL of the released medium was removed and replaced with 10 mL of fresh medium. The cumulative release of manganese ions was monitored using ICP-OES7200 (ThermoFisher, USA).

Fenton-like reaction activity of MQ

3,3′,5,5′-Tetramethylbenzidine (TMB) was employed as the substrate to monitor the generation of ·OH. Firstly, different concentrations of MQ (100, 80, 60, 40, 20, 10, 5, 1, 0 µg/mL) were added to varying concentrations of H_2O_2 (5, 2, and 1 mM). Subsequently, TMB solution (0.2 mM) was introduced and incubated at 37 °C. After 30 min, the UV–vis absorption spectra at 650 nm was recorded using a Microplate Reader (Victor Nivo™, PerkinElmer, USA).

In Vitro photothermal performance

To evaluate the photothermal performance of MQ, an 808 nm laser was used to trigger photothermal effect. Different concentrations of MQ (0, 31.2, 62.5, 125, 250 µg/mL) were irradiated with a NIR laser (808 nm, 1 W/cm^2) for 5 min. The temperature and thermal imaging were recorded every 60 s. After 5 min of irradiation, the laser was turned off, and the MQ samples were allowed to cool down to their initial temperature before the laser was applied again. This process was repeated for 3 cycles, and the temperature was recorded.

Cell viability assays in vitro

Hepa1-6 and THLE-2 cells were seeded at a density of 5000 cells per well in 96-well plates and incubated for 24 h. Following this incubation, varying concentrations of $MnCl_2$, Que, and MQ were added to the wells according to the experimental design. For experiments involving irradiation, after incubating with cells for 8 h, the cells were exposed to 808 nm laser light at a power density of 1 W/cm^2 for 5 min. Cell viability was subsequently assessed using the CCK-8 assay.

Cellular uptake behavior

To assess the cellular uptake of MQ, Hepa1-6 cells were cultured in well plates for 24 h. The uptake behavior of MQ by Hepa1-6 cells was evaluated using flow cytometry (FCM) and inverted fluorescence microscopy (Axiovert. A1, GER). Briefly, Hepa1-6 cells were incubated with RhB labeled MQ for various durations (0, 1, 2, 4, and 8 h) to investigate time-dependent uptake. For fluorescence microscopy, cells were washed with fresh PBS and observed under an inverted fluorescence microscope to determine the localization of MQ within the cells. Prior to observation, nuclei were stained with Hoechst 33,342 (10 µg/mL) for 10 min. For FCM analysis, cells were also incubated with RhB labeled MQ for the same time points (0, 1, 2, 4, and 8 h), and fluorescence intensity was measured. The excitation and emission wavelengths used were 544 nm and 627 nm, respectively.

Intracellular ROS detection

Hepa1-6 cells were seeded into well plates and allowed to grow for 24 h. Afterwards, the cells were subjected to various treatments: G1 (Control), G2 ($MnCl_2$: 17.5 µg/mL), G3 (Que: 8.5 µg/mL), G4 (NIR), G5 (MQ: 50 µg/mL), and G6 (MQ + NIR). Following treatment, the cells were then incubated with a 2′,7′-dichlorofluorescein diacetate (DCFH-DA) probe for 30 min. For the NIR and MQ + NIR groups, after incubating with cells for 8 h, cells were exposed to 808 nm laser light at a power density of 1 W/cm^2 for 5 min. Subsequently, fluorescence intensity was measured using FCM. For fluorescence microscopy, cell samples were stained with Hoechst 33,342 for 10 min, then washed twice with PBS. The stained samples were visualized under a fluorescence microscope to evaluate intracellular ROS level.

GSH assay

The ThiolTracker™ Violet dye was utilized to quantify the glutathione (GSH) content in Hepa1-6 cells. Firstly, Hepa1-6 cells were seeded in 24-well plates and incubated for 24 h. Following this, cells were subjected to various treatments (G1: Control, G2: MnCl$_2$, G3: Que, G4: NIR, G5: MQ, G6: MQ + NIR). The concentration of manganese ions, Que and MQ were 17.5 μg/mL, 8.5 μg/mL and 50 μg/mL, respectively. Afterwards, the cells were stained with ThiolTracker™ Violet dye (20 μM) for 30 min in the dark. After staining, the cells were washed with PBS and visualized using an inverted fluorescence microscope to assess GSH levels.

Mitochondrial membrane potential assay

To assess changes in mitochondrial membrane potential, Hepa1-6 cells were seeded in 24-well plates and cultured overnight. The cells were then subjected to various treatments (G1: Control, G2: MnCl$_2$, G3: Que, G4: NIR, G5: MQ, G6: MQ + NIR). The concentrations of each group were the same as before. Following treatment, the original culture medium was removed, and cells were washed with PBS. Fresh culture medium was added, and 1 mL of JC-1 staining working solution was introduced. The cells were then incubated at 37 °C for 20 min. After incubation, the cells were washed twice with JC-1 staining buffer to remove unbound dye. Mitochondrial changes were visualized using an inverted fluorescence microscope. Red fluorescence excitation and emission wavelengths of 585 nm and 590 nm, respectively. The excitation and emission wavelengths of green fluorescence were 514 nm and 529 nm, respectively.

Live/dead cells staining assay

Hepa1-6 cells were seeded in 6-well plates at a density of 1 × 10^5 cells per well and cultured for 24 h. Afterwards, the cells were treated with the following groups: Control, MnCl$_2$: 17.5 μg/mL, Que: 8.5 μg/mL, NIR, MQ: 50 μg/mL, and MQ + NIR. After a 24-h incubation, the culture medium was removed, and the cells were washed with PBS. For staining, the cells were treated with Calcein AM and propidium iodide (PI) for 20 min. Live and dead cells were visualized and quantified using an inverted fluorescence microscope.

Detection of cell apoptosis

Hepa1-6 cells were seeded in 6-well plates at a density of 1 × 10^5 cells per well and incubated for 24 h. Following this incubation, the cells were subjected to various treatments and divided into the following groups: Control, MnCl$_2$, Que, NIR, MQ, and MQ + NIR. The concentrations of each group are consistent with those used in previous experiments. After treatment, the cells were washed with PBS, digested with trypsin, centrifuged, and resuspended to obtain a single-cell suspension. For apoptosis analysis, cells were stained with 5 μL of Annexin V-FITC solution for 10 min at 4 °C in the dark, followed by 10 μL of PI solution for 5 min at 4 °C. Apoptotic cells were quantified using a flow cytometer (BECKMAN B51503 CytoFLEX, Beckman Coulter Trading (China) Co., Ltd.).

Detection of ATP

Hepa1-6 cells were seeded in 6-well plates and subjected to different treatments. After 24 h, the supernatant was collected separately, centrifuged, and extracellular ATP levels were measured using an ATP assay kit according to the manufacturer's instructions.

In vitro maturation of DC2.4 cells

Bone marrow-derived dendritic cells DC2.4 and Hepa1-6 cells were seeded in Transwell plates, with Hepa1-6 cells in the upper chamber and DC2.4 cells in the lower chamber, and incubated overnight. Hepa1-6 cells were then treated for 8 h with the following groups: Control, MnCl$_2$, Que, NIR, MQ, and MQ + NIR. The concentration of manganese ions, Que and MQ were 17.5 μg/mL, 8.5 μg/mL and 50 μg/mL, respectively. The NIR and MQ + NIR groups were irradiated with an 808 nm laser (1 W/cm^2) for 5 min. After treatment, Hepa1-6 cells were co-incubated with DC2.4 cells for 24 h. DC2.4 cells were then collected and stained with anti-CD11c, anti-CD80, and anti-CD86 antibodies. The percentage of CD11c$^+$CD80$^+$CD86$^+$ cells was analyzed by flow cytometry.

In vivo treatment experiment

Hepa1-6 (Luc1) cells were implanted subcutaneously in mice, and treatment was initiated when the tumor volume reached about 50 mm^3. Mice were randomly divided into six groups (n = 5): G1: PBS, G2: MnCl$_2$, G3: Que, G4: NIR, G5: MQ, G6: MQ + NIR. Then, mice were injected with the different formulations (G1: PBS, G2: $MnCl_2$, G3: Que, G4: PBS + NIR, G5: MQ, G6: MQ + NIR) via the tail vein on days 0, 3, 6, and 9. The concentrations of $MnCl_2$, Que and MQ injected into the mice were 1.75 mg/kg, 0.85 mg/kg and 5 mg/kg, respectively. Mice in the G4 and G6 groups were additionally irradiated with an 808 nm laser (1 W/cm^2) for 5 min, 24 h after formulation administration. Tumor size and body weight were monitored throughout the treatment. Meanwhile, bioluminescence imaging (PerkinElmer, USA) was used to monitor tumor volume changes in C57BL/6 mice. On the 18th day, euthanasia was performed on the mice, followed by the collection and analysis of tumors, lymph nodes, and major organs. Tumor tissues were assessed by immunofluorescence staining (TUNEL, γ-H2AX, p-STING), immunohistochemistry (cGAS), Western blotting, and flow cytometry (CD3, CD8). The maturity of dendritic cells (DCs) in the lymph nodes of mice was assessed using flow cytometry, focusing on the expression levels of CD11c, CD80, and CD86. Major organs (heart, liver, spleen, lungs, and kidneys) were stained with H&E, and serum was collected for ELISA assays.

To establish a murine model of tumor metastasis, Hepa1-6 cells were initially injected subcutaneously on the right flank of the mice to serve as the primary tumor. When the tumor volume reached ~ 50 mm^3, the mice were randomly divided into two groups (n = 5): the Control group and the MQ + NIR group. The MQ + NIR group was administered MQ (5 mg/kg) via tail vein injection on days 0, 3, 6, and 9, while the Control group was injected with PBS. The mice in the MQ + NIR group received irradiation with 808 nm NIR light at a dose of 1 W/cm^2, 24 h after MQ administration. On day 11, to simulate metastasis, Hepa1-6 cells were inoculated subcutaneously on the left flank of the mice, creating secondary tumors. Throughout the study, tumor size and body weight were monitored to assess the progression of the primary and metastatic tumors. On day 18, the mice were euthanized, and tumor tissues were harvested for further analysis. Flow cytometry was employed to evaluate immune cell infiltration within the tumors, specifically assessing the populations of CD3 and CD8 cells.

In the third batch of experiments, mice were randomly divided into four groups (n = 5): G1: PBS, G2: α-CTLA-4 (5 mg/kg), G3: MQ + NIR, G4: MQ + NIR + α-CTLA-4. PBS or MQ was injected via the tail vein on days 0, 3, 6, and 9. α-CTLA-4 was administered on days 1, 4, 7, and 10. Mice were irradiated as the above described.

In addition, Survival analysis was performed on 10 mice per group over a 40-day period, with endpoints defined as tumor volume reaching 1500 mm^3 or death.

Flow cytometric analysis

At the end of treatment, inguinal lymph nodes from tumor-bearing mice were excised and placed in 1 mL PBS. The lymph nodes were homogenized using the plunger of a 1 mL syringe until the suspension became turbid. The resulting cell suspension was filtered through a 40 μm cell sieve to remove tissue debris and then centrifuged at 800 g for 5 min. The cells were resuspended in 5% BSA solution and incubated for 15 min to block non-specific binding. Subsequently, the cells were stained with CD11c, CD80, and CD86 antibodies for 30 min in the dark. Flow cytometric analysis was performed to evaluate the activation of dendritic cells (DCs) in the lymph nodes.

For the analysis of immune cells infiltration in tumor tissue, tumors were excised and minced in 2 mL RPMI-1640 medium. The tissues were further digested with type IV collagenase (1 mg/mL), hyaluronidase (0.2 mg/mL), and DNAse I (0.2 mg/mL) for 1 h at 37 °C in a water bath. After digestion, the suspension was filtered through a 40 μm cell sieve and centrifuged at 800 g for 5 min. The cell pellet was then mixed with Percoll at a 2:1 ratio, layered onto a Percoll gradient, and centrifuged at 20 °C for 20 min. The interface containing the viable cells was collected, washed with PBS, and blocked with 5% BSA for 15 min. The single-cell suspension was then stained with anti-CD3 and anti-CD8 antibodies for 30 min. Flow cytometry was employed to assess immune cells infiltration within the tumor.

Statistical analysis

Statistical analyses were conducted using GraphPad Prism software (version 9). One-way or two-way analysis of variance (ANOVA) or Student's *t* test were used for inter-group comparisons. Data were presented as mean ± standard deviation (SD). The level of significance in the statistical analyses was defined as $^{*}p < 0.05$, $^{**}p < 0.01$, $^{***}p < 0.001$, and $^{****}p < 0.0001$.

Results and discussion

Preparation and characterization of dual-modality immune nano-activator

To synthesize the Mn-Que coordination-based Nano-Activator (MQ), $MnCl_2{\cdot}4H_2O$ was mixed with an ethanol solution of Que in an alkaline environment at room temperature. During the stirring process, the solution exhibited a sequential color transition from yellow to brown, and finally to black, which served as an indicative sign of the successful synthesis of MQ. Additionally, the Mn loading content within MQ, quantified at approximately 34.30 ± 6.18%, provided robust evidence for the effective incorporation of Mn into the MQ structure. TEM

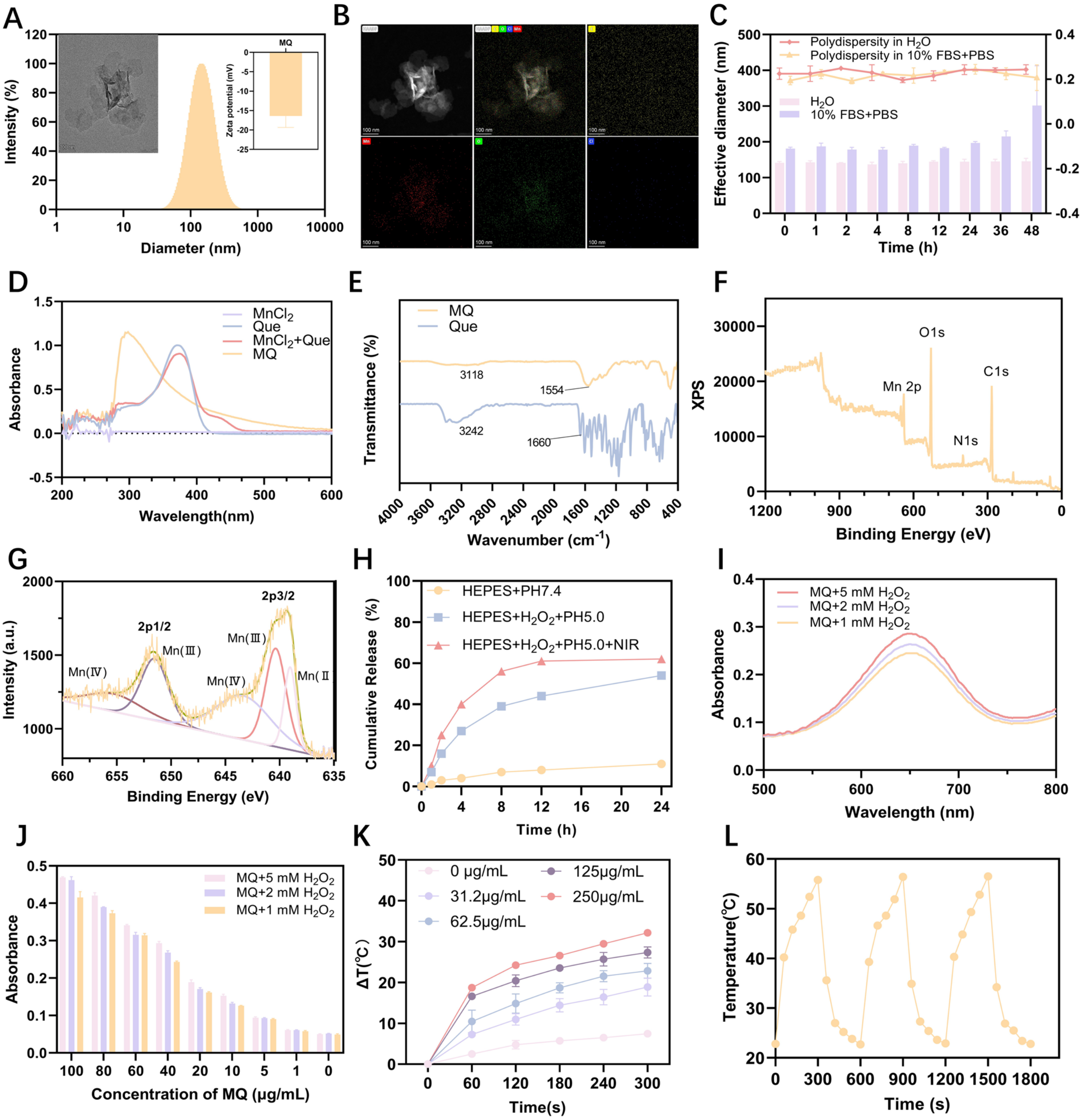

Fig. 1 Characterization of the physicochemical properties of MQ. **a** TEM image, diameter and zeta potential of MQ (scale bars: 100 nm); **b** TEM image and elemental mapping of MQ (scale bars: 100 nm); **c** The stability of MQ in different solutions; **d** UV–Vis spectra of different agents and MQ; **e** FT-IR spectra of Que and MQ; **f** XPS spectrum of MQ; **g** XPS analysis of the multiple valence states of Mn in MQ; **h** Cumulative release of Mn from MQ under different conditions; **i** UV–Vis spectra of MQ at different concentrations of H_2O_2; **j** UV–Vis spectra of MQ at different concentrations; **k** The temperature change curves of different concentrations of MQ under 808 nm irradiation; **l** The temperature curves of MQ after 3 irradiation cycles

analysis revealed the presence of petal-like nanostructures in MQ. Dynamic light scattering (DLS) measurements showed that the average size of MQ was about 141 nm, with a zeta potential of about −16 mV (Fig. 1a). Elemental mapping images confirm the successful preparation of MQ (Fig. 1b). Notably, MQ exhibited minimal size fluctuations in both H_2O and 10%FBS + PBS solutions, indicating its robust stability under both storage and physiological conditions (Fig. 1c). Furthermore, the metal–ligand coordination interaction between Que and manganese ions was evaluated using UV–Vis spectroscopy. As shown in Fig. 1d, the maximum absorption

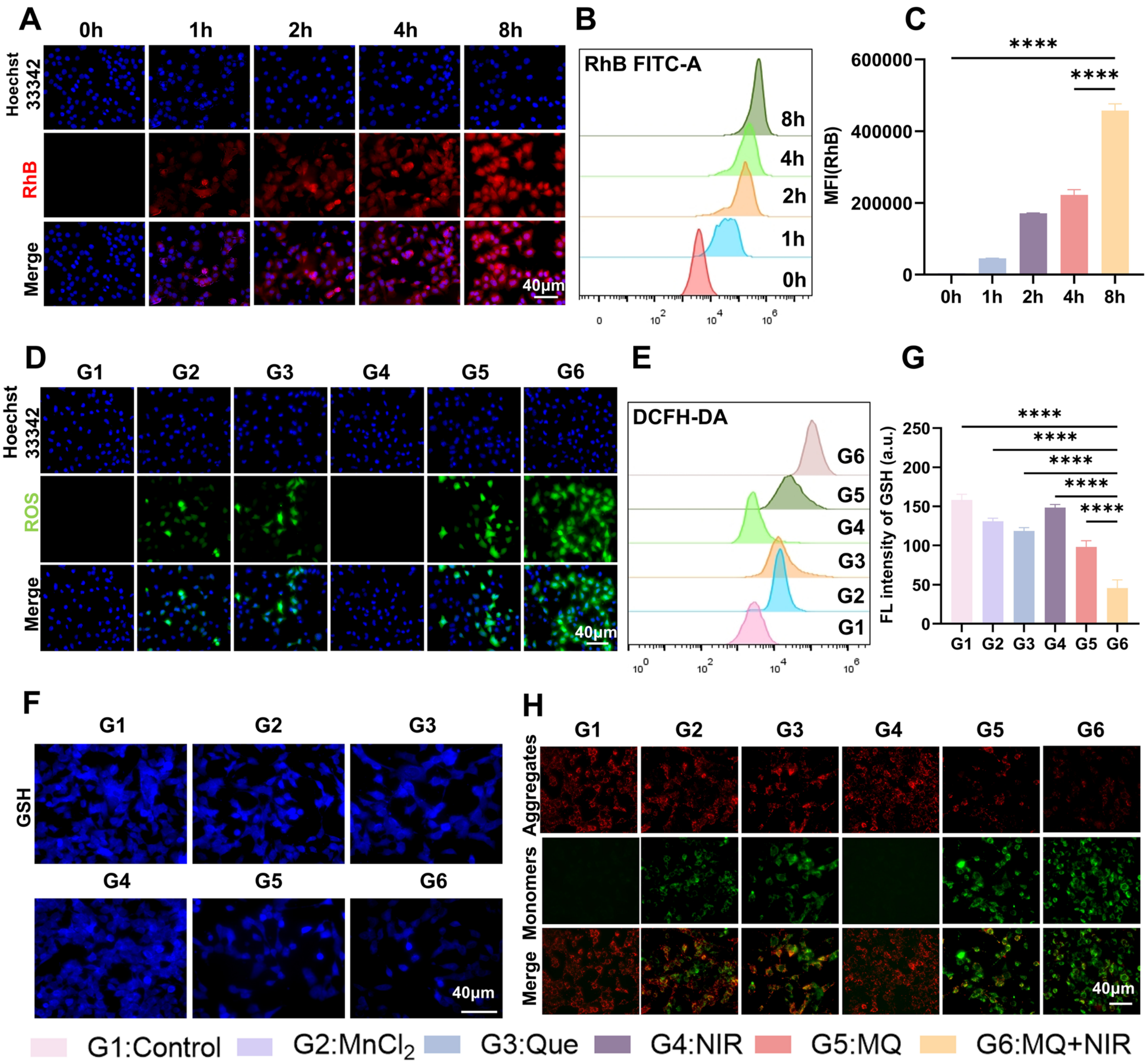

Fig. 2 In vitro cellular uptake of MQ and its synergistic effects on oxidative damage in tumor cells. **a** Fluorescence inverted microscopy images depicting the cellular uptake of MQ at 0, 1-, 2-, 4- and 8-h post-incubation. **b** Flow cytometry analysis of cellular uptake efficiency of MQ. **c** Quantitative data of MQ uptake capability from FCM, presented as mean ± SD (n = 3). **d** Intracellular ROS levels assessed using the DCFH-DA probe (green), with nuclei stained by Hoechst33342 (blue). **e** Analysis of intracellular ROS levels by flow cytometry. **f** Fluorescence microscopy images showing glutathione (GSH) staining in Hepa1-6 cells following various treatments. **g** Semi-quantitative analysis of GSH levels derived from fluorescence microscopy images of Hepa1-6 cells after different treatments. **h** Fluorescence inverted microscopy images illustrating changes in mitochondrial membrane potential in Hepa1-6 cells. Data were presented as mean ± SD (n = 3). Statistical significance was determined using one-way ANOVA. **p* < 0.05, ***p* < 0.01, ****p* < 0.001, *****p* < 0.0001. "ns" indicated no significant difference. Abbreviations: GSH, glutathione; ROS, reactive oxygen species

peak of Que was at 372 nm, while that of MQ shifted to 298 nm, likely due to the complexation of manganese ions with Que (Fig. 1d). This observation was further corroborated by Fourier Transform Infrared (FT-IR) spectroscopy, as depicted in Fig. 1e. Specifically, the peak in the 3000–3500 cm^{-1} range of Que, attributed to –OH stretching vibrations, exhibited a weakening, broadening, and a shift to lower frequencies in MQ, confirming the coordination between –OH groups and manganese ions. Additionally, the sharp peak at about 1660 cm^{-1} in Que, assigned to $-C=O$ stretching, was weakened in MQ, further demonstrating the successful coordination of manganese ions with Que (Fig. 1e). The XPS spectra analysis

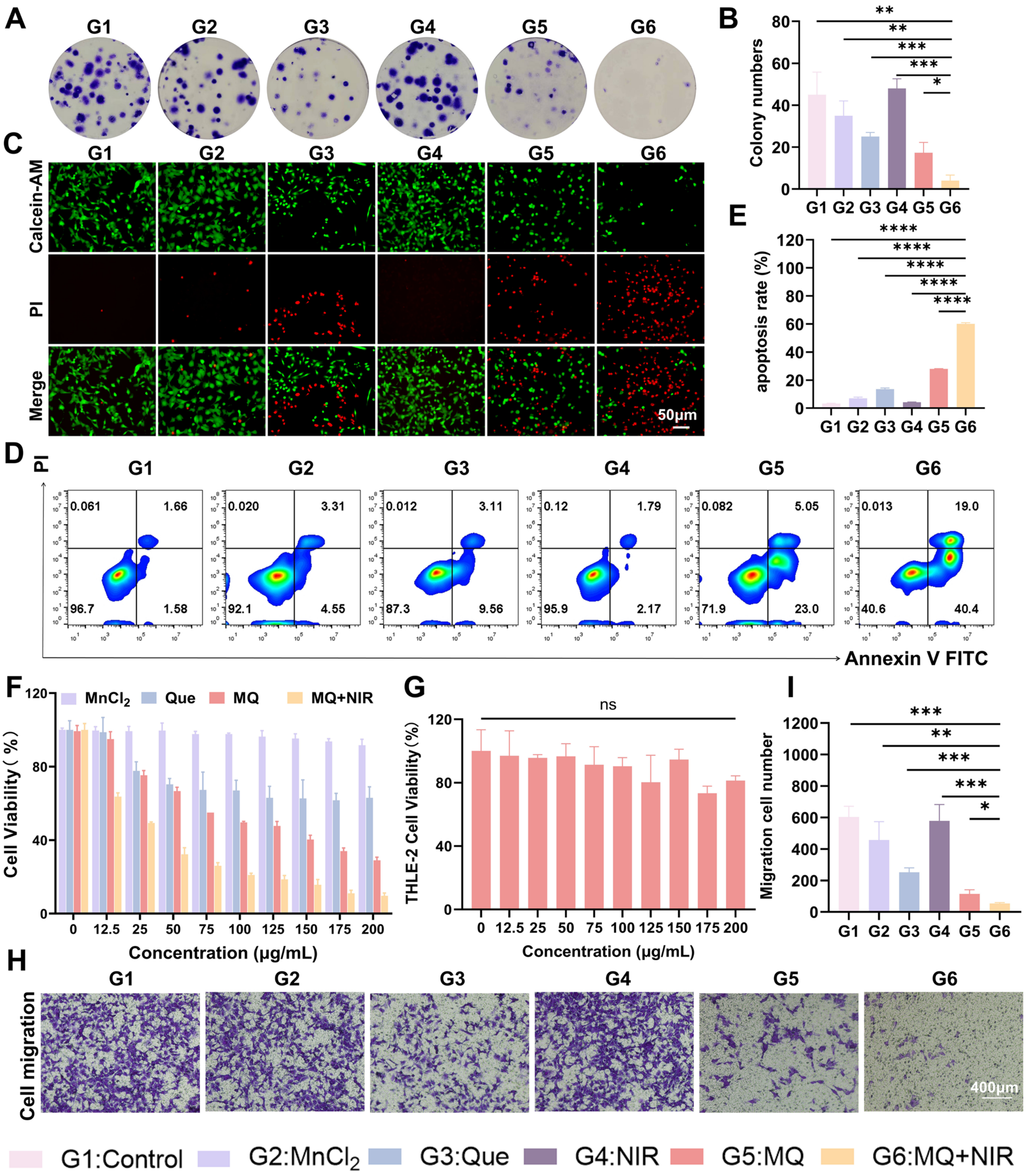

Fig. 3 Antitumor effects of MQ combined with NIR irradiation on the proliferation and apoptosis of Hepa1-6 cells. **a** Colony Formation assay assessing the proliferation of Hepa1-6 cells following various treatments. **b** Quantitative assessment of cell proliferation in the respective treatment groups. **c** Calcein-AM and PI staining to visualize live (green fluorescence) and dead (red fluorescence) cells in different treatment groups. **d** Flow cytometry (FCM) analysis of Hepa1-6 cells after treatment, showing dual staining with PI and Annexin V FITC. **e** Apoptosis rates in different treatment groups. **f** Cell survival rates of Hepa1-6 cells after different treatments. **g** Cell viability of THLE-2 cells treated with different concentrations of MQ + NIR. **h** Detection of the migratory capacity of cells in each treatment group and **i** quantitative analysis of the number of migrating cells. Data were presented as mean ± SD (n = 3). Statistical analysis was performed using one-way ANOVA or Student's *t* test to determine differences between groups. *$p < 0.05$, **$p < 0.01$, ***$p < 0.001$, ****$p < 0.0001$. "ns" indicated no significant difference

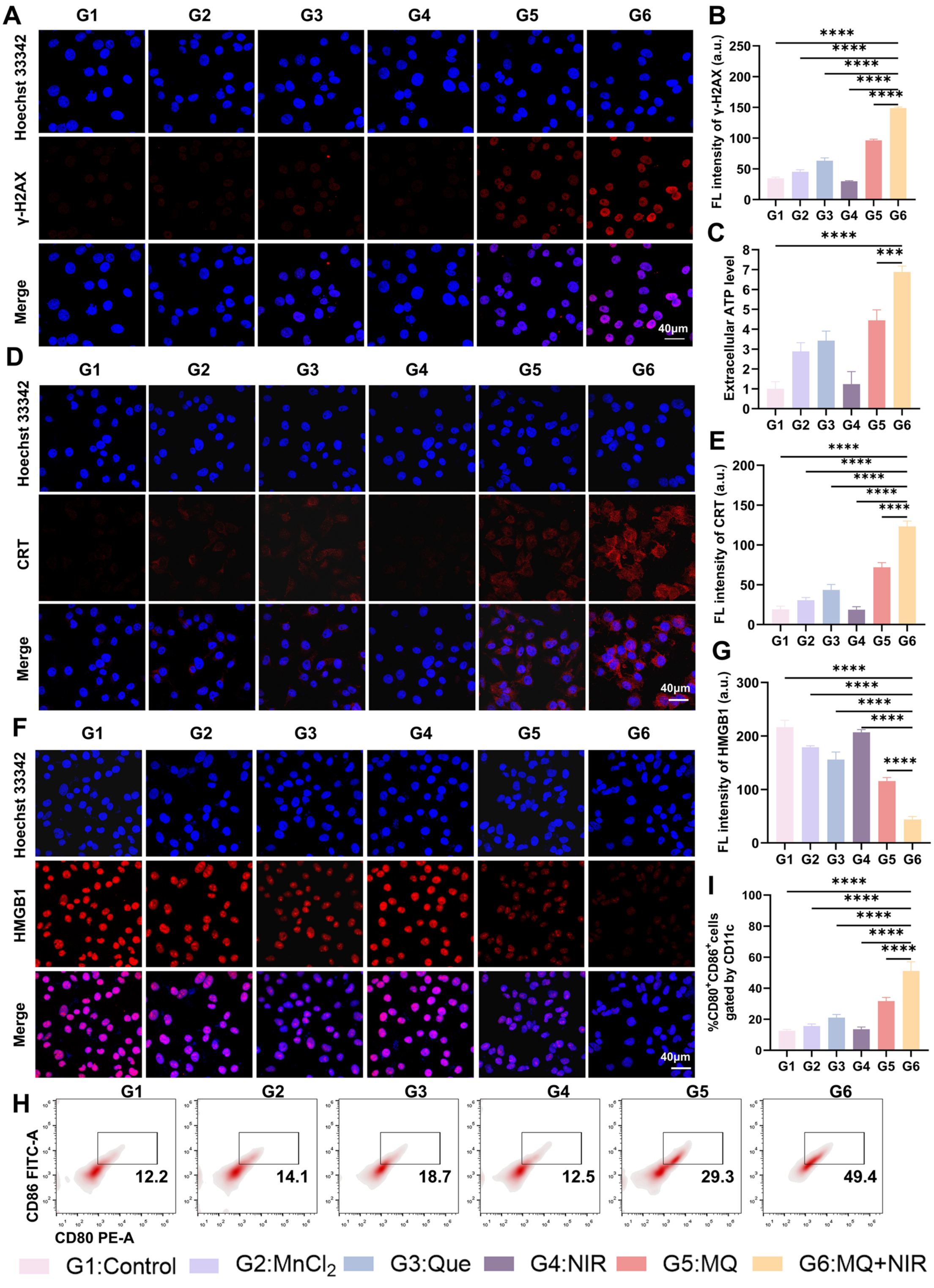

Fig. 4 MQ-induced ICD effects and dendritic cells maturation. **a** CLSM images showing γ-H2AX labeling of cellular DNA damage in Hepa1-6 cells; **b** semi-quantitative analysis of γ-H2AX staining; **c** ATP secretion levels in Hepa1-6 tumor cells under different treatments; **d** CLSM images of CRT localization on the cell membranes of Hepa1-6 cells in various treatment groups; **e** Semi-quantitative analysis of CRT immunofluorescence; **f** Immunofluorescence detection of extracellularly released HMGB1; **g** Semi-quantitative analysis of extracellular HMGB1 release; **h** Flow cytometry analysis of mature dendritic cells in different treatment groups; **i** Quantitative data of mature dendritic cells obtained from FCM. Statistical differences between groups were analyzed using one-way ANOVA or Student's *t* test. $*p < 0.05$, $**p < 0.01$, $***p < 0.001$, $****p < 0.0001$. "ns" indicated no significant difference

demonstrated the presence of Mn in MQ, as indicated by the peaks associated with Mn (Fig. 1f). Notably, The XPS spectral analysis provided further confirmation of the presence of Mn in multiple valence states within MQ, as illustrated in Fig. 1g. This finding suggested that MQ possessed the capability to deplete glutathione (GSH) and facilitate the production of reactive oxygen species (ROS), highlighting its potential application in redox-related biological processes [47].

To evaluate the capacity of MQ to generate hydroxyl radicals (·OH), a Fenton-like reactivity assessment was conducted using 3,3′,5,5′-Tetramethylbenzidine (TMB), a dye that underwent a color change from colorless to blue upon reaction with ·OH. As shown in Fig. 1i, an obvious absorption peak at 650 nm was observed after MQ incubated with H_2O_2 and TMB, with the absorbance intensity increasing as the concentration of H_2O_2 increased. Similarly, an increasing trend in absorbance was observed with elevated MQ concentrations (Fig. 1j). These results indicated that MQ possessed the ability to consume H_2O_2 and produce ·OH at tumor site, ultimately leading to tumor cells death through a Fenton-like reaction mechanism. Given the potential photothermal conversion capability of MQ, an assessment of its photothermal effect was conducted by monitoring the temperature changes in MQ suspensions of different concentrations. Representative thermal imaging and quantitative results both showed that a significant temperature elevation with prolonged irradiation time as well as increased MQ concentration. In contrast, the control group exhibited negligible temperature variations (Fig. 1k and Figure S1). Notably, MQ at the concentration of 250 μg/mL achieved a temperature increase to 55.3 °C, which was sufficient to kill tumor cells, indicating its potential for tumor destruction through efficient photothermal conversion. Moreover, after three irradiation cycles for 5 min, the heating curve of MQ remained consistent, indicating good photostability (Fig. 1l). More importantly, NIR irradiation of MQ accelerated the release of Mn ions (Fig. 1h). In the presence of high concentrations of H_2O_2 within tumor cells, NIR irradiation increased the cumulative release of Mn ions compared to conditions without NIR irradiation. This observation underscored the ability of our engineered nano-activators to rapidly release Mn ions within tumor cells, thereby maximizing their therapeutic efficacy. Overall, MQ not only exhibited Fenton-like reaction activity but also showed excellent photothermal conversion efficiency and rapid release of functional molecules within tumor cells, positioning it as a promising therapeutic agent in the field of cancer nanomedicine.

In vitro oxidative stress capacity evaluation

The therapeutic efficacy of the MQ in cancer treatment was primarily determined by its efficient cellular uptake by tumor cells, a critical step for inducing cytotoxic effects. To explore this, Rhodamine B (RhB) was employed as a fluorescent probe. Fluorescent inverted microscope images revealed a time-dependent increase in MQ uptake, with the peak accumulation observed after 8 h of incubation (Fig. 2a). This observation was further validated by flow cytometry analysis (Fig. 2b, c), confirming the remarkable intracellular uptake efficiency of MQ. Notably, upon internalization, the MQ nano-activators were found to induce the production of reactive oxygen species (ROS) within the cells. Although quercetin, a component of the nano-activator, was known for its antioxidant properties and its ability to scavenge free radicals in normal cells, it often exhibited pro-oxidative effects in tumor cells [48]. To assess ROS generation, the DCFH-DA probe was used to measure intracellular ROS levels. The results demonstrated that both $MnCl_2$ and Que, when applied individually, led to an increase in ROS levels. However, the MQ treatment group exhibited a significantly higher level of intracellular ROS, particularly when combined with NIR irradiation (Fig. 2d and Figure S2). These findings suggested that MQ enhanced ROS generation through Fenton-like reactions by facilitating the release of Mn ions in the acidic tumor microenvironment. Moreover, the multivalent states of Mn in MQ contributed to amplified ROS production (Fig. 2e and Figure S3) by disrupting cellular redox homeostasis, primarily

(See figure on next page.)

Fig. 5 In Vivo Anti-Tumor Efficacy of MQ combined with NIR irradiation. **a** In vivo fluorescence images of Hepa1-6 tumor-bearing mice at different time points after intravenous injection of Cy5.5 and MQ@Cy5.5; **b** Average fluorescence intensity of tumors and major organs isolated from mice in corresponding in vivo fluorescence images. **c** Overview of the experimental procedures for evaluating in vivo anti-tumor effects in C57BL/6 female Hepa1-6 (Luc1) tumor-bearing mice. **d** Bioluminescence imaging of tumor growth at different time points. **e** Tumor growth curves over time for each treatment group. **f** Tumor weights post-treatment in each group of Hepa1-6 mice. **g** Body weight changes in mice across different treatment groups. Data were presented as mean ± SD (n = 5). **h** Survival rates of Hepa1-6 tumor-bearing mice following different treatments, shown over time (n = 10). **i** Hematoxylin and eosin (H&E) staining of tumors from different groups. **j** TUNEL staining of tumor tissues isolated from various treatment groups. Statistical differences between groups were analyzed using two-way ANOVA or Student's *t* test. *$p < 0.05$, **$p < 0.01$, ***$p < 0.001$, ****$p < 0.0001$. "ns" indicated no significant difference

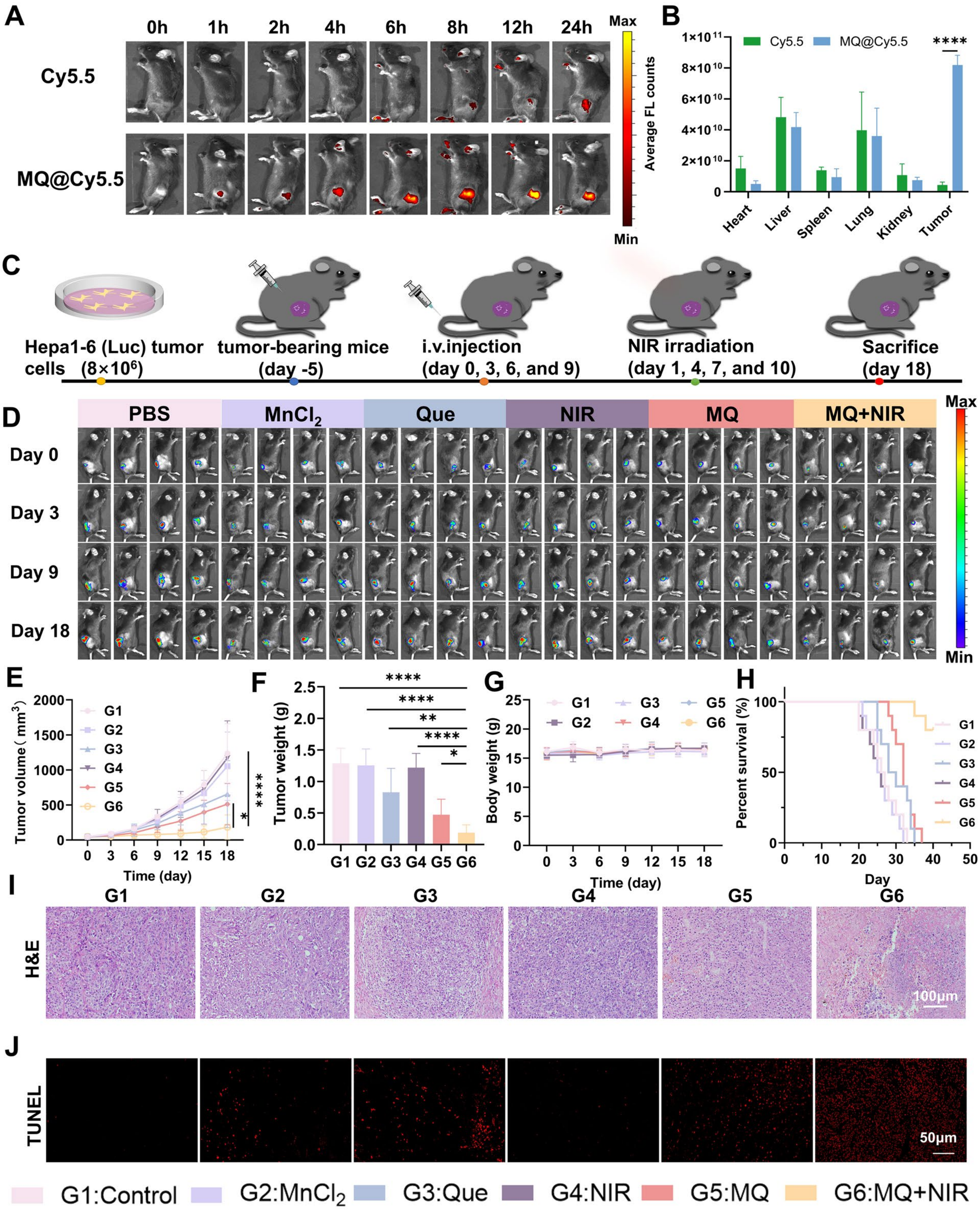

Fig. 5 (See legend on previous page.)

through the depletion of intracellular glutathione (GSH) (Fig. 2f, g). The observed significant decrease in mitochondrial membrane potential further supported the hypothesis that MQ, particularly in combination with photothermal therapy, may induce mitochondrial dysfunction (Fig. 2h and Figure S4). This dysfunction likely

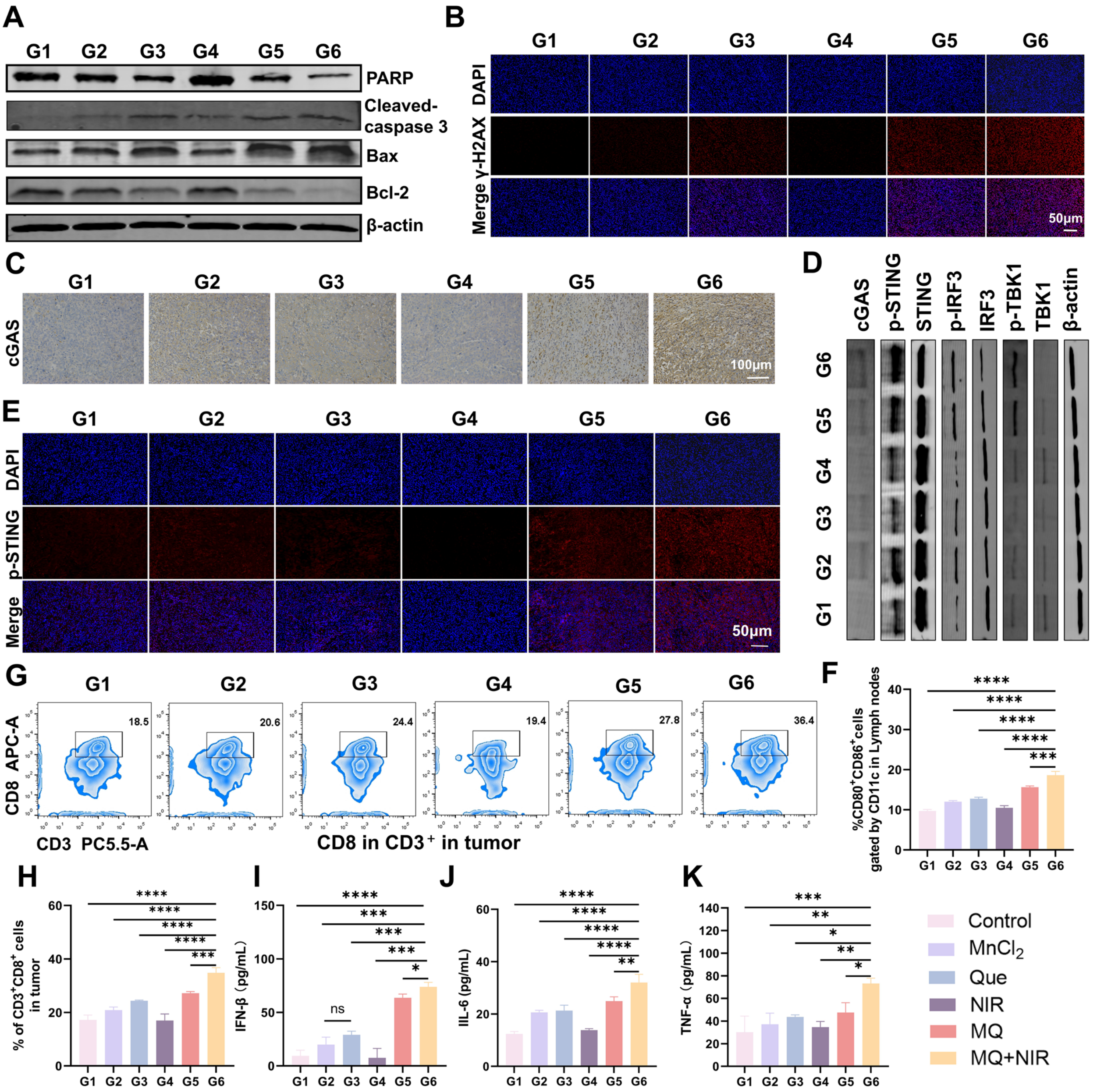

Fig. 6 In vivo immune response of MQ under NIR irradiation. **a** Western blot analysis showing the expression levels of various apoptosis-related proteins in Hepa1-6 (Luc1) tumors isolated from mice subjected to different treatments; (B, E) Fluorescence images of Hepa1-6 tumor sections stained with γ-H2AX and p-STING antibodies, respectively, demonstrating the presence of DNA damage and cGAS-STING pathway activation in tumors from different treatment groups; **c** Immunohistochemical analysis of tumor tissues from different treatment, highlighting specific markers related to the cGAS-STING pathway; **d** Western blot analysis for the detection of cGAS-STING pathway proteins in Hepa1-6 tumors from mice receiving various treatments, indicating changes in protein expression related to the pathway activation; **f** FCM patterns showing quantitative analysis of CD80$^+$ and CD86$^+$ expression on CD11c$^+$ mature dendritic cells in different treatment groups 18 days post-treatment; **g** FCM patterns and **h** quantitative analysis of CD8$^+$ T cells within the CD3$^+$ T cells population in different treatment groups after 18 days; (I-K) The levels of IFN-β, IL-6, and TNF-α in Hepa1-6 tumor-bearing mice after receiving different treatments on day 18. Data were expressed as mean ± SD (n = 3). Statistical differences between groups were analyzed using one-way ANOVA or Student's *t* test. *$p < 0.05$, **$p < 0.01$, ***$p < 0.001$, ****$p < 0.0001$. "ns" indicated no significant difference

triggered downstream apoptotic signaling pathways, including the release of mitochondrial DNA (mtDNA), accelerated apoptosis and cells death in tumor cells. Collectively, the MQ exhibited significant potential in cancer therapy due to their efficient cellular uptake, ability to induce oxidative stress, and promotion of mitochondrial dysfunction. These mechanisms collectively enhanced its effectiveness as an anti-tumor agent, offering promising avenues for cancer treatment strategies.

In vitro cytotoxicity of dual-modality immune nano-activator

Given the efficient generation of ROS and photothermal effect by MQ, we systematically evaluated the impact of various treatment on tumor cells proliferation using colony formation and EdU proliferation assays. The results revealed that MQ significantly inhibited tumor cells colony formation compared to free Que. This inhibitory effect was further enhanced when combined with NIR irradiation, as indicated by a notable reduction in the red fluorescence intensity of EdU-labeled proliferative cells (Figure S5). The colony formation results further supported these findings (Fig. 3a, b).

To further assess the cytotoxicity of MQ, live/dead cells staining assays were conducted. The results demonstrated that, while free Que induced moderate apoptosis due to its inherent antitumor activity, MQ exhibited a synergistic effect attributable to its unique photothermal effect and ROS generation, significantly enhancing anti-tumor efficacy (Fig. 3c). Specifically, the apoptosis rate in cells treated with MQ reached 28.05%, which increased to 59.4% upon NIR irradiation. These rates were significantly higher compared to those observed in the free Mn^{2+} (7.86%) and Que (12.67%) treatment groups, underscoring the superior efficacy of the engineered nano-activators (Fig. 3d, e). The result was further supported by TUNEL fluorescent staining, which revealed accelerated apoptosis in tumor cells due to the combined effects of ROS generation, the photothermal effect, and the intrinsic anti-tumor activity of Que (Figure S6). Additionally, MQ demonstrated greater inhibition of tumor cells proliferation compared to free Mn^{2+}, especially when combined with NIR irradiation. The inhibition of proliferation was found to be dependent on concentration (Fig. 3f). Nevertheless, while increasing the irradiation intensity from 1 W/cm^2 to 2 W/cm^2 did not significantly enhance tumor cells killing, 1 W/cm^2 was selected as the optimal irradiation intensity for MQ (Figure S7). These findings confirmed the effective antitumor activity of MQ. To assess the safety of MQ, toxicity studies were conducted on THLE-2 cells. Even at concentrations as high as 200 μg/mL, MQ showed negligible toxicity to THLE-2 cells (Fig. 3g), providing important safety assurance for potential clinical applications.

In addition to its antitumor effects, MQ significantly inhibited tumor migration and invasion. The transwell migration assay revealed that the MQ + NIR treatment group exhibited the lowest tumor migration rate, demonstrating its potent inhibitory capability (Fig. 3h, i). In the absence of NIR irradiation, the number of migrating cells nearly doubled, underscoring the critical role of the photothermal effect in migration inhibition. The scratch assay further supported these findings, showing that MQ substantially reduced tumor migration rates both with and without NIR irradiation. Specifically, at 48 h post-treatment, the migration rate in the combined NIR treatment group decreased to 4.3%, compared to 24.3% in the free Que treatment group (Figure S8). Thus, MQ effectively inhibited tumor proliferation through a synergistic mechanism and significantly reduced tumor migration, demonstrating its remarkable anti-tumor effects.

Dual-modality immune nano-activator initiated ICD effect and activate the cGAS-STING pathway

The MQ developed in this study exhibited remarkable efficacy in inducing tumor apoptosis, as evidenced by key apoptotic markers, including the nuclear condensation, fragmentation, and the cleavage of nuclear DNA. To evaluate the extent of DNA damage, γ-H2AX as a critical marker of the DNA damage was employed. Immunofluorescence staining demonstrated an increase in γ-H2AX expression following MQ treatment, which correlated with the proportion of apoptotic cells (Fig. 4a, b), thereby confirming the DNA damage induced by MQ. The accumulation of damaged DNA not only elevated cytoplasmic DNA levels but also acted as a signal to activate the cGAS-STING pathway.

To further explore the activation of cGAS-STING pathway, we assessed key proteins involved in this pathway, including cGAS, phosphorylated STING (p-STING) and phosphorylated IRF3 (p-IRF3). The results revealed a significant upregulation of cGAS (Figure S9), p-STING and p-IRF3 in cells after treated with MQ + NIR (Figures S10 and S11). This upregulation was attributed to the synergistic effects of MQ-induced ROS production and the photothermal effect, which enhanced DNA release and subsequently amplified the immunological effects induced by Mn^{2+}. These effects led to an increase in cGAS enzymatic activity and enhanced DNA-sensing capacity, facilitating the synthesis of cGAMP (cyclic GMP-AMP) and its effective binding to STING. Activation of the cGAS-STING pathway was essential for initiating anti-tumor immune responses and remodeling the TME. Considering the role of Mn^{2+} in activating the cGAS-STING pathway and generating hydroxyl radicals

(OH) through Fenton-like reactions, coupled with the ability of Que to induce apoptosis, we further investigated MQ-induced immunogenic cell death (ICD). ICD markers, such as ATP release, HMGB1 release, and calreticulin (CRT) translocation to the cell surface, were measured. The MQ treatment group exhibited a significant increase in extracellular ATP levels (Fig. 4c), which was essential for recruiting immature dendritic cells (DCs). Additionally, there was also a notable increase in HMGB1 release (Fig. 4f, g), and immunofluorescence staining revealed CRT exposure on the cell membrane (Fig. 4d, e). As shown in Fig. 4h, i, these changes collectively facilitated DC maturation. In summary, the engineered MQ effectively induced the release of ICD-associated marker and activated the cGAS-STING pathway, highlighting their potential as potent anti-tumor agents capable of efficiently promoting DC maturation in vitro.

In vivo antitumor effect

To assess the antitumor efficacy of MQ in vivo, we firstly evaluated its biodistribution. Following the administration of Cy5.5-labled MQ and free Cy5.5, the fluorescence signal from the Cy5.5-labled MQ at the tumor site was significantly stronger than that from free Cy5.5, attributable to the enhanced permeability and retention (EPR) effects. The fluorescence intensity reached its peak at 12 h post-injection, indicating a notably superior accumulation of MQ in the tumor compared to free Cy5.5 (Fig. 5a and Figure S12). Tissue distribution analysis conducted 24 h post-injection revealed that MQ predominantly accumulated in the tumor, lungs, and liver (the main metabolic organs), affirming its effective tumor-targeting capability and potential for anti-tumor therapy (Fig. 5b and Figure S13). Moreover, a significant temperature increase was observed in the MQ-treated group, with a peak temperature of 52.7 °C within 5 min of irradiation, further validating the tumor targeting ability of MQ and providing a solid foundation for its subsequent anti-tumor treatment (Figure S14).

The anti-tumor efficacy of MQ in combination with NIR irradiation was further evaluated in a Hepa1-6 subcutaneous xenograft tumor model in mice. The specific therapeutic protocols were outlined in Fig. 5c. Mice with tumors of approximately 50 mm^3 in volume were treated with various formulations, including PBS, $MnCl_2$, Que and MQ. After multiple rounds of injection and NIR irradiation, the MQ + NIR group exhibited the most pronounced tumor growth inhibition. The fluorescence intensity in this group was notably lower than that in the $MnCl_2$ or Que groups, with NIR irradiation further enhancing the antitumor effects (Fig. 5d). The tumor growth curves supported the potent anti-tumor effects of the MQ + NIR treatment, likely due to a synergistic antitumor mechanism (Fig. 5e). At the end of the treatment, the tumor weight and volume were consistent with these results (Fig. 5f). More importantly, the mice maintained stable body weights and exhibited no significant toxic side effects (Fig. 5g), with over 80% of the mice surviving beyond 40 days, in contrast to shorter survival times observed in the other groups due to limited therapeutic efficacy (Fig. 5h). H&E analysis further supported these findings. As shown in Fig. 5i, H&E staining revealed the most significant tumor necrosis in the MQ + NIR group, while TUNEL staining demonstrated the highest apoptosis rate in this group (Fig. 5j). These observations were consistent with the in vitro data, collectively underscoring the superior efficacy of MQ combined with NIR irradiation.

To assess the biological safety of MQ, we first performed a detailed hemocompatibility evaluation. Co-incubation of MQ at various concentrations with blood cells revealed that MQ, similar to the control group, exhibited very low hemolysis rates, indicating its safety in blood circulation (Figure S15). To evaluate its in vivo systemic toxicity, MQ was intravenously administered to healthy mice. The analysis of hematological markers, including blood routine parameters as well as liver and kidney function, revealed no significant differences between the MQ-treated mice and the healthy controls (Figure S16). In addition, H&E staining of major organs at the end of treatment showed no significant lesions, inflammatory responses, or morphological alterations (Figure S17), further demonstrating that MQ possessed excellent biocompatibility and safety, supporting

(See figure on next page.)

Fig. 7 In Vivo Anti-Tumor Efficacy of MQ + NIR combined with α-CTLA-4 antibody in Hepa1-6 tumor-bearing mice. **a** Schematic representation of the in vivo anti-tumor study, including the inoculation of Hepa1-6 (Luc1) cells into C57BL/6 mice. **b** Bioluminescence imaging for monitoring tumor progression across different treatment groups; **c** Time-dependent tumor growth curves for the four treatment groups; **d** Tumor weights measured from mice in each treatment group; **e** Changes in body weight of mice following treatments in each group. Data were presented as mean ± SD, n = 5. **f** Survival rates of Hepa1-6 tumor-bearing mice over time for each treatment group, n = 10. **g** Flow cytometry (FCM) analysis patterns and **h** quantitative percentages of CD8$^+$ cells among CD3$^+$ T cells after 18 days of treatment in each group. n = 3. **i** Serum levels of TNF-α and **j** IFN-γ on day 18 post-treatment for the different groups, n = 3. Statistical significance was determined using one-way or two-way ANOVA or Student's *t* test. *$p < 0.05$, **$p < 0.01$, ***$p < 0.001$, ****$p < 0.0001$. "ns" indicated no significant difference

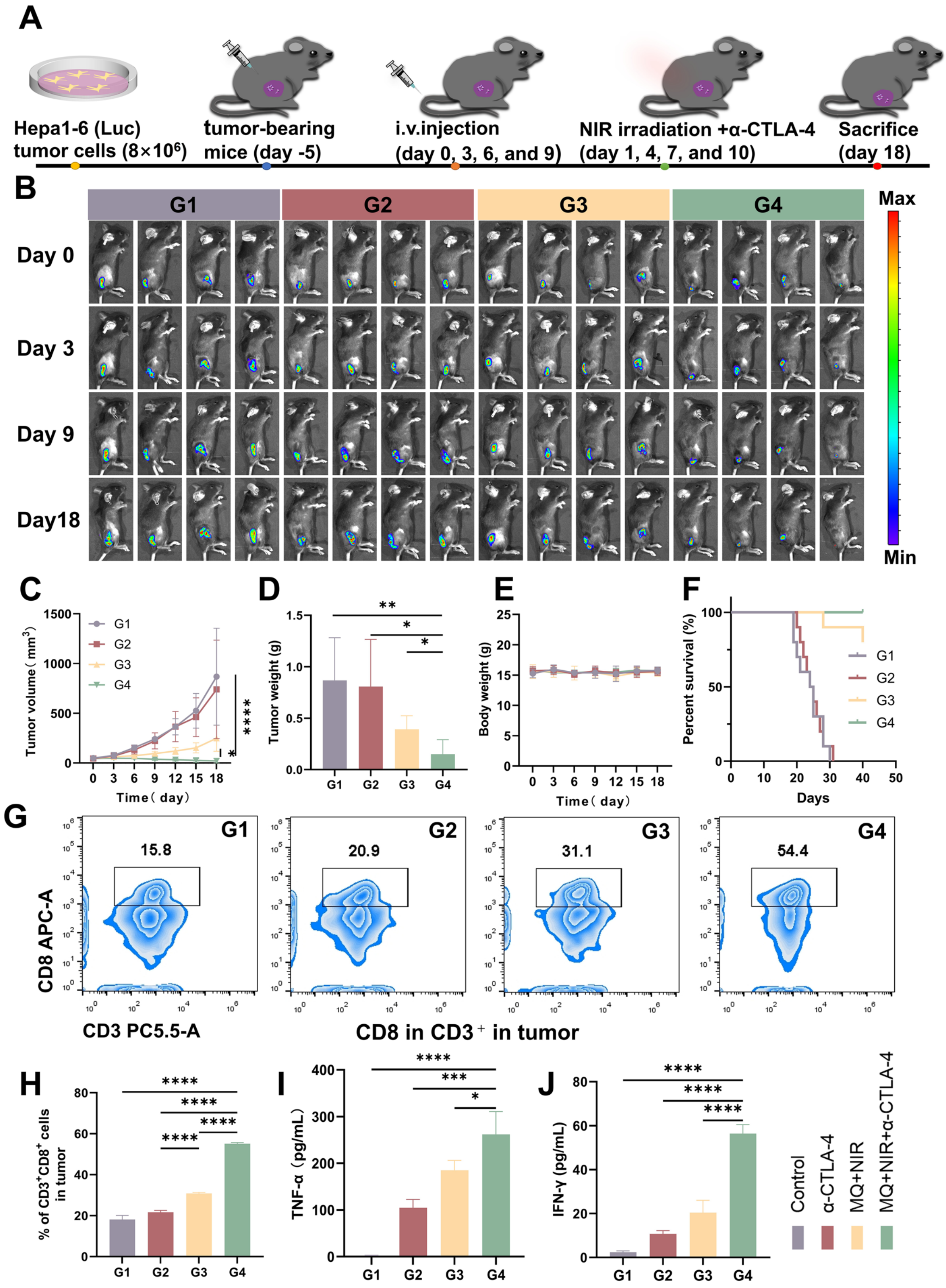

Fig. 7 (See legend on previous page.)

its potential for further clinical development and application.

In vivo antitumor immune activation and antitumor metastatic evaluation

To investigate the antitumor immune response induced by MQ and its underlying mechanisms, we extracted proteins from tumor tissues across various treatments groups and systematically analyzed them using Western blot (WB). Previous in vitro studies confirmed that MQ could induce apoptosis in tumor cells, promoting us to focus on key proteins associated with classical apoptotic pathways. Results showed that, in the MQ + NIR group, anti-apoptotic proteins such as PARP and Bcl-2 were significantly downregulated, whereas the pro-apoptotic protein Bax was markedly upregulated, accompanied by increased cleavage of caspase-3. These findings provided robust evidence of apoptosis occurring in tumor cells after MQ treatment (Fig. 6a and Figure S18). Additionally, we employed immunofluorescence staining to assess γ-H2AX expression, a marker of DNA damage. Results indicated significantly elevated γ-H2AX levels in the nuclei of tumor cells treated with MQ + NIR, which was consistent with in vitro findings and indicative of substantial DNA damage. The damaged DNA fragments were subsequently released into the cytoplasm, serving as critical signals for activating the cGAS-STING pathway (Fig. 6b and Figure S19). In the cytoplasm, DNA fragments were initially recognized by cGAS. Our study revealed a significant increase in cGAS expression in the MQ + NIR group, particularly in the presence of Mn^{2+}. This enhancement was attributed to the combined effects of MQ's direct pro-apoptotic activity, photothermal effect and the production of ROS (Fig. 6c). Mn^{2+} not only enhanced cGAS sensitivity to DNA but also promoted STING activation. Given the superior tumor-targeting ability and in vivo circulation stability of MQ, the Mn^{2+} released in the MQ + NIR group effectively enhanced p-STING expression (Fig. 6e and Figure S20). Phosphorylation of TBK1 and IRF3, key downstream regulatory proteins in the cGAS-STING pathway, was crucial for pathway activation. WB analysis revealed significantly higher levels of p-TBK1 and p-IRF3 in the MQ and MQ + NIR treatment groups compared to other groups. In contrast, free Mn^{2+} and Que, due to their limited bioavailability, did not effectively induce phosphorylation of TBK1 and IRF3 (Fig. 6d and Figure S21). These results, corroborated by immunohistochemistry and immunofluorescence analyses, further underscored the critical role of MQ in activating the cGAS-STING pathway.

To evaluate the in vivo immune response, we examined the immune cells composition in tumors and lymph nodes using flow cytometry (FCM). Results revealed a significant increase in the proportion of mature dendritic cells ($CD80^+CD86^+$) in the lymph nodes of the MQ and MQ + NIR groups, which were 1.71-fold and 2.08-fold higher, respectively, compared to the control group. This increase suggested an enhanced antigen presentation capability (Fig. 6f and Figure S22). Simultaneously, there was a notable increase in $CD8^+$ T cell ($CD3^+CD8^+$) infiltration within the tumor tissues, particularly in the MQ + NIR group, where the proportion of $CD8^+$ T cells was 1.97-fold higher than in the control group. This suggested the enhanced immune response contributed to the observed inhibition of tumor growth (Fig. 6g, h). Furthermore, the elevated levels of IFN-β and cGAMP in the serum of treated mice indicated activation of the cGAS-STING pathway (Fig. 6i and Figure S23). The concentrations of IFN-β in the serum of mice treated with MQ and MQ + NIR group were several-fold higher than those in the control group, confirming the effective activation of the cGAS-STING pathway and a robust innate immune response. Additionally, the combination of MQ with NIR irradiation promoted the release of pro-inflammatory cytokines IL-6 and TNF-α, further enhancing the antitumor immune response (Fig. 6j, k). In all, the combination of MQ with NIR irradiation effectively facilitated DC maturation and $CD8^+$ T cell infiltration through the activation of the cGAS-STING pathway, thereby eliciting a potent anti-tumor immune response.

To comprehensively evaluate the efficacy of immune response activation on tumor metastasis, we established a mouse tumor metastasis model. As shown in Figure S24, a unilateral subcutaneous tumor graft was fist implanted in mice, followed by consistent antitumor treatment. On day 11, Hepa1-6 tumor cells were inoculated contralateral to simulate tumor metastasis. Consistent with the previous results, the primary tumor (designated as the first tumor) showed significant growth inhibition after treatment (Figure S24), whereas no significant changes in body weight were observed in all experimental groups throughout the monitoring period. Notably, the growth rate of the contralateral tumor (designated as the second tumor) was significantly slowed after treatment with MQ combined with NIR irradiation, compared to the control group. Moreover, $CD8^+$T cells in contralateral tumor tissues were detected by flow cytometry, and $CD8^+$T cell in MQ + NIR group was significantly increased. This finding highlighted the treatment's ability to impact metastatic sites beyond the primary tumor.

In vivo antitumor evaluation combined with α-CTLA-4

Cytotoxic T lymphocyte-associated antigen 4 (CTLA-4) acted as a critical negative regulator of immune responses. Checkpoint inhibitors, such as anti-CTLA-4 antibodies (α-CTLA-4), have been clinically approved for cancer immunotherapy. These inhibitors function by counteracting the immunosuppressive effects of regulatory T cells (Tregs), thereby enhancing the antitumor immune response. Given the remarkable anti-tumor immune responses induced by MQ + NIR, we hypothesized that the combination of MQ + NIR with α-CTLA-4 could further enhance anti-cancer efficacy. To test this hypothesis, we established a subcutaneous xenograft tumor model in mice by inoculating Hepa1-6 (Luc1) cells unilaterally. MQ was administered via tail vein injections on days 0, 3, 6, and 9, followed by NIR irradiation to activate the anti-tumor immune response (Fig. 7a). Tumor growth was continuously monitored to evaluate the efficacy of these combined treatments. Results demonstrated that the MQ + NIR + α-CTLA-4 combination therapy significantly reduced bioluminescence signals compared to both the control group and the α-CTLA-4 monotherapy group, reflecting a reduction in tumor burden and demonstrating the effectiveness of the combination therapy (Fig. 7b). Further analysis showed that the combination therapy resulted in the smallest increases in tumor volume and weight, providing strong evidence for enhanced anti-tumor efficacy (Fig. 7c, d). Notably, although α-CTLA-4 antibody alone had a limited impact on tumor growth inhibition, its combination with MQ + NIR therapy markedly overcame this limitation, significantly extending survival, with a 100% survival rate at all monitored time points and a survival duration exceeding 40 days (Fig. 7f). Additionally, no significant changes in body weight were observed among the treatment groups, indicating the overall safety of the treatment regimens (Fig. 7e).

To further elucidate the underlying anti-tumor mechanisms of the combination therapy, we evaluated immune cell infiltration within the tumor microenvironment. Flow cytometry analysis revealed that the percentage of $CD8^+$ T cells in the combination therapy group was 54.4%, approximately 2.6 times higher than in the α-CTLA-4-only group (20.9%) (Fig. 7g, h). Moreover, this group showed a significant increase in the secretion of pro-inflammatory cytokines TNF-α and IFN-γ, which were crucial for inducing tumor cells apoptosis, enhancing immune cells cytotoxicity, and facilitating immune memory, thereby contributing to effective tumor eradication (Fig. 7i, j). Collectively, the synergistic effect of MQ + NIR therapy combined with α-CTLA-4 antibody activated $CD8^+$ T cells and increased pro-inflammatory cytokine secretion, resulting in effective tumor growth inhibition and notable survival extension. These findings presented a novel strategy for advancing cancer immunotherapy.

Conclusion

In this study, we have successful developed a dual-modality immune nano-activator that combined Mn^{2+} and Que to enhance the activation of the cGAS-STING pathway for tumor immunomodulation. The rationally designed nanosystems demonstrated three key advantages: (1) improved tumor-targeting ability and enhanced cellular uptake efficiency; (2) synergistic integration of PTT and multi-pathway immune activation, wherein NIR irradiation not only induced tumor cell apoptosis but also facilitated the release of manganese ions and Que; and (3) self-amplifying therapeutic cascades, where the released manganese ions promoted ROS generation, which in combination with Que, exacerbated photothermal-induced DNA damage and cytosolic DNA accumulation, leading to the activation of the cGAS-STING pathway. Notably, the nano-activator induced ICD, which worked together with the activation of GAS-STING pathway to promote DC maturation and facilitated the generation of robust tumor-specific cytotoxic T lymphocyte (CTL) responses. Furthermore, the therapeutic efficacy was significantly enhanced when combined with anti-CTLA-4 antibodies. Collectively, this work introduced a paradigm-shifting strategy that transcended conventional STING agonism by integrating metal ion-mediated pathway activation with phytochemical-driven immune modulation, offering a promising approach for advancing tumor immunotherapy.

Supporting information available

Experimental sections including materials and methods, and supplementary Figures S1-S24 are provided in Supporting Information.

Supplementary Information

The online version contains supplementary material available at https://doi.org/10.1186/s12951-025-03336-8.

Additional file 1

Acknowledgements
Not applicable.

Author contributions
Shanshan Ma: Formal analysis, Writing-Original Draft; Xuequan Zhang: Conceptualization, Formal analysis; Xiaoqi Zhu: Methodology, Software; Kangning Yan and Qin Wang: Date Curation; Lei Lei and Jiasheng Li: Investigation, Validation; Jing Guo, Weizhong Tang and Junjie Liu: Supervision, Validation, Funding acquisition; Jun Cao: Conceptualization, Project administration; Duo Wang: Supervision, Resources, Funding acquisition; Tao Luo: Writing—review and editing;

Funding
We acknowledge funding by the National Natural Science Foundation of China (82402408 and 82160341), Postdoctoral Fellowship Program of CPSF (BX20230068), China Postdoctoral Science Foundation (2024M750452 and 2022M710852), Guangxi Natural Science Foundation Key Project (2022GXNSFDA035060), Guangxi Science and Technology Base and Talent Special Program (AD19245197), Guangxi Key Laboratory of Early Prevention and Treatment for Regional High-Frequency Tumor, and Guangxi liver cancer Diagnosis and treatment engineering technology Research Center.

Data availability
No datasets were generated or analysed during the current study.

Declarations

Ethics approval and consent to participate

All animal experiments have been approved by Guangxi Medical University Cancer Hospital's Ethical Committee with an approval number: LW2024068.

Competing interests

The authors declare no competing interests.

Author details

[1]Department of Medical Ultrasound, Guangxi Medical University Cancer Hospital, Guangxi Medical University, No. 71 Hedi Road, Nanning 530021, People's Republic of China. [2]National Engineering Research Center for Biomaterials, College of Biomedical Engineering, Sichuan University, No. 29 Wangjiang Road, Chengdu 610064, People's Republic of China. [3]Center of Interventional Radiology & Vascular Surgery, Department of Radiology, Zhongda Hospital, Medical School. Southeast University, No. 87 Dingjiaqiao, Nanjing 210009, People's Republic of China. [4]Guangxi Key Laboratory of Early Prevention and Treatment for Regional High Frequency Tumor, Guangxi Medical University, No. 22 Shuangyong Road, Nanning 530021, People's Republic of China. [5]Department of Gastrointestinal Surgery, Guangxi Medical University Cancer Hospital, Guangxi Medical University, No. 71 Hedi Road, Nanning 530021, People's Republic of China.

Received: 29 October 2024 Accepted: 16 March 2025

References

1. Wang D, Zhang M, Zhang Y, Qiu G, Chen J, Zhu X, et al. Intraparticle double-scattering-decoded sonogenetics for augmenting immune checkpoint blockade and CAR-T therapy. Adv Sci. 2022;9(32): e2203106.
2. Wang D, Zhang M, Qiu G, Rong C, Zhu X, Qin G, et al. Extracellular matrix viscosity reprogramming by in situ au bioreactor-boosted microwave-genetics disables tumor escape in CAR-T immunotherapy. ACS Nano. 2023;17(6):5503–16.
3. Wang Y, Yang L, Yan C, Du Y, Li T, Yang W, et al. Supramolecular artificial Nano-AUTACs enable tumor-specific metabolism protein degradation for synergistic immunotherapy. Sci Adv. 2024;10(25):eadn8079.
4. Lei L, Huang D, Gao H, Cao J, Peppas NA. Hydrogel-guided strategies to stimulate an effective immune response for vaccine-based cancer immunotherapy. Sci Adv. 2022;8(47):eadc8738.
5. Qin L, Cao J, Shao K, Tong F, Yang Z, Lei T, et al. A tumor-to-lymph procedure navigated versatile gel system for combinatorial therapy against tumor recurrence and metastasis. Sci Adv. 2020;6(36):eabb3116.
6. He Y, Lei L, Cao J, Yang X, Cai S, Tong F, et al. A combinational chemo-immune therapy using an enzyme-sensitive nanoplatform for dual-drug delivery to specific sites by cascade targeting. Sci Adv. 2021;7(6):eaba0776.
7. Xiao Y, Yu D. Tumor microenvironment as a therapeutic target in cancer. Pharmacol Ther. 2021;221: 107753.
8. Guo X, Tu P, Wang X, Du C, Jiang W, Qiu X, et al. Decomposable nanoagonists enable NIR-elicited cGAS-STING activation for tandem-amplified photodynamic-metalloimmunotherapy. Adv Mater. 2024;36(21): e2313029.
9. Wang Y, Luo J, Alu A, Han X, Wei Y, Wei X. CGAS-STING pathway in cancer biotherapy. Mol Cancer. 2020;19(1):136.
10. Wan D, Jiang W, Hao J. Research advances in how the cGAS-STING pathway controls the cellular inflammatory response. Front Immunol. 2020;11:615.
11. Jiang M, Jiang M, Chen P, Chen P, Wang L, Li W, et al. CGAS-STING, an important pathway in cancer immunotherapy. J Hematol Oncol. 2020;13(1):81.
12. Samson N, Ablasser A. The cGAS–STING pathway and cancer. Nat Cancer Nature Res. 2022;3(12):1452–63.
13. Du H, Xu T, Cui M. cGAS-STING signaling in cancer immunity and immunotherapy. Biomed Pharmacother. 2021;133: 110972.
14. Zheng J, Mo J, Zhu T, Zhuo W, Yi Y, Hu S, et al. Comprehensive elaboration of the cGAS-STING signaling axis in cancer development and immunotherapy. Mol Cancer. 2020;19(1):133.
15. Chen Q, Sun L, Chen ZJ. Regulation and function of the cGAS-STING pathway of cytosolic DNA sensing. Nat Immunol. 2016;17(10):1142–9.
16. Shen R, Liu D, Wang X, Guo Z, Sun H, Song Y, et al. DNA damage and activation of cGAS/STING pathway induce tumor microenvironment remodeling. Front Cell Dev Biol. 2022;9: 828657.
17. Won JK, Bakhoum SF. The cytosolic DNA-sensing cGAS–sting pathway in cancer. Cancer Discov. 2020;10(1):26–39.
18. Aikins ME, Sun X, Dobson H, Zhou X, Xu Y, Lei YL, et al. STING-activating cyclic dinucleotide-manganese nanoparticles evoke robust immunity against acute myeloid leukemia. J Control Release. 2024;368:768–79.
19. Woo SR, Fuertes MB, Corrales L, Spranger S, Furdyna MJ, Leung MYK, et al. STING-dependent cytosolic DNA sensing mediates innate immune recognition of immunogenic tumors. Immunity. 2014;41:830–42.
20. Ishikawa H, Barber GN. STING is an endoplasmic reticulum adaptor that facilitates innate immune signalling. Nature. 2008;455:674–8.
21. Sun X, Huang X, Park KS, Zhou X, Kennedy AA, Pretto CD, et al. Self-assembled STING-activating coordination nanoparticles for cancer immunotherapy and vaccine applications. ACS Nano. 2024;18:10439–53.
22. Garland KM, Sheehy TL, Wilson JT. Chemical and biomolecular strategies for STING pathway activation in cancer immunotherapy. Chem Rev. 2022;122(6):5977–6039.
23. Wang D, Deng X, Wang J, Che S, Ma X, Zhang S, et al. Environmentally responsive hydrogel promotes vascular normalization to enhance STING anti-tumor immunity. J Control Release. 2024;372:403–16.
24. Wang D, Nie T, Huang C, Chen Z, Ma X, Fang W, et al. Metal-cyclic dinucleotide nanomodulator-stimulated STING signaling for strengthened radioimmunotherapy of large tumor. Small. 2022;18(41): e2203227.
25. Ding C, Song Z, Shen A, Chen T, Zhang A. Small molecules targeting the innate immune cGAS-STING-TBK1 signaling pathway. Acta Pharm Sin B. 2020;10(12):2272–98.
26. Chin EN, Yu C, Vartabedian VF, Jia Y, Kumar M, Gamo AM, et al. Antitumor activity of a systemic STING-activating non-nucleotide cGAMP mimetic. Science. 2020;369(6506):993–9.
27. Yang J, Luo Z, Ma J, Wang Y, Cheng N. A next-generation STING agonist MSA-2: from mechanism to application. J Control Release. 2024;371:273–87.
28. Yang L, Wang Y, Song Y, Li Z, Lei L, Li H, et al. Metal coordination nanotheranostics mediated by nucleoside metabolic inhibitors potentiate STING pathway activation for cancer metalloimmunotherapy. J Control Release. 2024;370:354–66.
29. Meng Y, Huang J, Ding J, Zhou H, Li Y, Zhou W. Mn-phenolic networks as synergistic carrier for STING agonists in tumor immunotherapy. Mater Today Bio. 2024;26: 101018.
30. Qiao W, Chen J, Zhou H, Hu C, Dalangood S, Li H, et al. A single-atom manganese nanozyme Mn-N/C promotes anti-tumor immune response via eliciting type I interferon signaling. Adv Sci. 2024;11(14): e2305979.
31. Li Q, Yang M, Sun X, Wang Q, Yu B, Gong A, et al. NIR responsive nanoenzymes via photothermal ablation and hypoxia reversal to potentiate the STING-dependent innate antitumor immunity. Mater Today Bio. 2023;19: 100566.
32. Hu Z, Song X, Ding L, Cai Y, Yu L, Zhang L, et al. Engineering Fe/Mn-doped zinc oxide nanosonosensitizers for ultrasound-activated and multiple ferroptosis-augmented nanodynamic tumor suppression. Mater Today Bio. 2022;16: 100452.
33. Gao F, Sun M, Zhang J, Chang Y, Gao W, Ma G, et al. Fenton-like reaction and glutathione depletion by chiral manganese dioxide nanoparticles for enhanced chemodynamic therapy and chemotherapy. J Colloid Interface Sci. 2022;616:369–78.
34. Zhao Y, Pan Y, Zou K, Lan Z, Cheng G, Mai Q, et al. Biomimetic manganese-based theranostic nanoplatform for cancer multimodal imaging and twofold immunotherapy. Bioact Mater. 2023;19:237–50.
35. Feng Y, Liu Y, Ma X, Xu L, Ding D, Chen L, et al. Intracellular marriage of bicarbonate and Mn ions as "immune ion reactors" to regulate redox homeostasis and enhanced antitumor immune responses. J Nanobiotechnology. 2022;20(1):193.
36. Wang P, Wang Y, Li H, Wang M, Wang Y, Wang X, et al. A homologous-targeting cGAS-STING agonist multimodally activates dendritic cells for enhanced cancer immunotherapy. Acta Biomater. 2024;177:400–13.

37. Du Q, Luo Y, Xu L, Du C, Zhang W, Xu J, et al. Smart responsive Fe/Mn nanovaccine triggers liver cancer immunotherapy via pyroptosis and pyroptosis-boosted cGAS-STING activation. J Nanobiotechnology. 2024;22(1):95.
38. Qin J, Guo N, Yang J, Chen Y. Recent advances of metal-polyphenol coordination polymers for biomedical applications. Biosensors (Basel). 2023;13(8):776.
39. Bu Z, Yang J, Zhang Y, Luo T, Fang C, Liang X, et al. Sequential ubiquitination and phosphorylation epigenetics reshaping by MG132-Loaded Fe-MOF disarms treatment resistance to repulse metastatic colorectal cancer. Adv Sci (Weinh). 2023;10(23): e2301638.
40. Suliman IH, Kim K, Chen W, Kim Y, Moon JH, Son S, et al. Metal-based nanoparticles for cancer metalloimmunotherapy. Pharmaceutics. 2023;15(7):2003.
41. Sun Y, Zheng L, Yang Y, Qian X, Fu T, Li X, et al. Metal-organic framework nanocarriers for drug delivery in biomedical applications. Nanomicro Lett. 2020;12(1):103.
42. Yang J, Yang YW. Metal-organic frameworks for biomedical applications. Small. 2020;16(10): e1906846.
43. Li L, Zhang M, Liu T, Li J, Sun S, Chen J, et al. Quercetin-ferrum nanoparticles enhance photothermal therapy by modulating the tumor immunosuppressive microenvironment. Acta Biomater. 2022;154:454–66.
44. Reyes-Farias M, Carrasco-Pozo C. The anti-cancer effect of quercetin: molecular implications in cancer metabolism. Int J Mol Sci. 2019;20(13):3177.
45. Tang SM, Deng XT, Zhou J, Li QP, Ge XX, Miao L. Pharmacological basis and new insights of quercetin action in respect to its anti-cancer effects. Biomed Pharmacother. 2020;121: 109604.
46. Hu K, Miao L, Goodwin TJ, Li J, Liu Q, Huang L. Quercetin remodels the tumor microenvironment to improve the permeation, retention, and antitumor effects of nanoparticles. ACS Nano. 2017;11(5):4916–25.
47. Lin LS, Song J, Song L, Ke K, Liu Y, Zhou Z, et al. Simultaneous fenton-like ion delivery and glutathione depletion by MnO2-based nanoagent to enhance chemodynamic therapy. Angewandte Chemie Int Ed. 2018;57:4902–6.
48. Wang ZX, Ma J, Li XY, Wu Y, Shi H, Chen Y, et al. Quercetin induces p53-independent cancer cell death through lysosome activation by the transcription factor EB and Reactive Oxygen Species-dependent ferroptosis. Br J Pharmacol. 2021;178:1133–48.

Publisher's Note